Letter Vol. 4, No. 10 / October 2017 / Optica 1228

optica

High performance monolithic, broadly tunable mid-infrared quantum cascade lasers

Wenjia Zhou, Donghai Wu, Ryan McClintock, Steven Slivken, and Manijeh Razeghi*

Center for Quantum Devices, Department of Electrical Engineering and Computer Science, Northwestern University, Evanston, Illinois 60208, USA
**Corresponding author: razeghi@eecs.northwestern.edu*

Received 26 April 2017; revised 8 September 2017; accepted 11 September 2017 (Doc. ID 294708); published 10 October 2017

Mid-infrared lasers, emitting in the spectral region of 3–12 μm that contains strong characteristic vibrational transitions of many important molecules, are highly desirable for spectroscopy sensing applications. High-efficiency quantum cascade lasers have been demonstrated with up to watt-level output power in the mid-infrared region. However, the wide wavelength tuning that is critical for spectroscopy applications still largely relies on incorporating external gratings, which have stability issues. Here, we demonstrate a monolithic, broadly tunable quantum cascade laser source emitting between 6.1 and 9.2 μm through an on-chip integration of a sampled grating distributed feedback tunable laser array and a beam combiner. High peak power up to 65 mW has been obtained through a balanced high-gain active region design, efficient waveguide layout, and the development of a broadband antireflection coating. Nearly fundamental transverse-mode operation is achieved for all emission wavelengths with a pointing stability better than 1.6 mrad (0.1°). The demonstrated laser source opens new opportunities for mid-infrared spectroscopy.

OCIS codes: (140.5965) Semiconductor lasers, quantum cascade; (140.3600) Lasers, tunable; (140.3298) Laser beam combining; (300.6340) Spectroscopy, infrared.

https://doi.org/10.1364/OPTICA.4.001228

Tunable laser spectroscopy in the mid-infrared (MIR, $3 < \lambda < 12$ μm) holds great potential for a variety of sensing applications, including explosives detection, breath analysis, and environmental monitoring. Quantum cascade lasers (QCLs) based on bandgap engineering of semiconductor structures have now become a standard coherent light source in the MIR thanks to its compact size and ability to operate at room temperature [1]. QCLs based on the InP material system are developed across the entire MIR region following the decoupling of the emission wavelength from the bandgap [2]. Single-mode QCLs with distributed feedback (DFB), which are excellent light sources for high-precision spectroscopy studies [3], are demonstrated with watt-level output power. However, widely tunable lasers are still highly desirable for scanning the absorption features in a wide spectral range to distinguish two chemicals that may have overlapping features at a certain wavelength.

Due to the intersubband nature of quantum cascade lasers, their optical gain typically has a single maximum at the emission energy, with little absorption at higher and lower energies (atomic-like behavior). As a result, a broadband MIR gain can be engineered by heterogeneously stacking together multiple QCL active regions emitting at different wavelengths [4–7]. The broadband laser core can then be combined with a wavelength-selecting mechanism to allow wavelength tuning over a wide range. Broadband tuning has been demonstrated [5,7] when coupled to an external grating. However, external cavity lasers have mechanical speed and stability issues and require alignment of multiple optical components to function. On the other hand, lasers utilizing sampled grating distributed feedback (SGDFB) technology have shown great promise for wide wavelength tuning without any external optical components [8–10]. When implemented in an array fashion, a broadband tuning was demonstrated and the multiple outputs of the laser array were combined via an on-chip beam combiner [11]. Here, we further develop the technique and demonstrate a high performance, monolithic, broadly tunable QCL between 6.1 and 9.2 μm. The output power is significantly increased by improving the broadband wafer gain, redesigning the waveguide layout and developing a broadband antireflection (AR) coating. Beam-shape measurement results reveal fundamental transverse-mode operation with a high pointing stability better than 1.6 mrad (0.1°).

Figure 1(a) shows the schematic structure of a broadband heterogeneous QCL. Five QCL subcores, each based on a four-well active region scheme, with peak gain wavelengths at 5.4, 5.9, 6.5, 7.4, and 8.4 μm are used to form the heterogeneous QCL core. The subcores are based on a strain-balanced $Al_{0.63}In_{0.37}As/Ga_{0.35}In_{0.65}As/Ga_{0.47}In_{0.53}As$ material system grown by gas-source molecular beam epitaxy (MBE) on an *n*-InP substrate. Figure 1(b) shows the conduction band diagram for one QCL stage emitting at 7.4 μm. In comparison to the wafer used in [11], the overlap between the upper laser level and the underlying energy levels was increased by decreasing the width of the first well of the active region, to increase the laser gain. This is accompanied by a decrease in the upper laser level lifetime from 1.55 ps to 1.35 ps and therefore an increase in the maximum operating current at the resonant electric field, for similar doping density. The number of stages for each laser core is optimized by

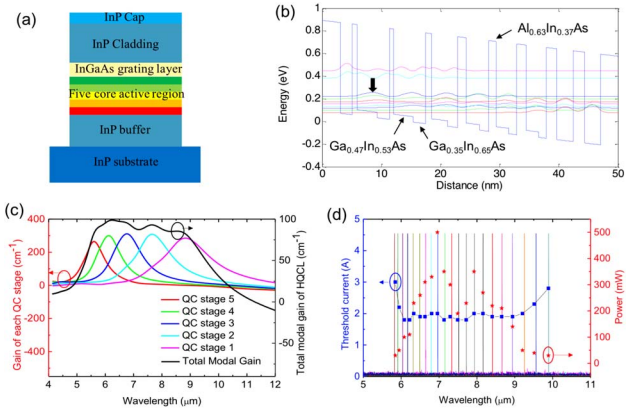

Fig. 1. (a) Schematic structure of the five-core heterogeneous QCL design. (b) A conduction band diagram and relevant energy levels of a QCL stage emitting at 7.4 μm based on the strain-balanced $Al_{0.63}In_{0.37}As/Ga_{0.35}In_{0.65}As/Ga_{0.47}In_{0.53}As$ material system. (c) An overlay plot of the simulated gain of each QCL stage designed for different wavelengths and the total modal gain at a current density of ~4 kA/cm^2. The loss at the long wavelength side (>10 μm) comes from intersubband absorptions within the mini-band. (d) An overlay plot of the compiled single-mode emission spectra of the DFB laser array, threshold current, and single-mode peak power as a function of wavelength.

considering the gain of each core and its optical confinement factor. As shown in Fig. 1(c), a relatively flat gain is achieved between 6–10 μm for a stage number of 12, 11, 10, 15, and 27 for the 5.4, 5.9, 6.5, 7.4, and 8.4 μm subcore, respectively. Compared to the design in [11], the gain is increased by 20% on average. The improved gain increases the dynamic range between the threshold and maximum operating currents and can improve the power output of the laser. Experimentally, the electroluminescence spectrum of the wafer has a full width at half-maximum (FWHM) of 870 cm^{-1}, centered at 1360 cm^{-1}. The broadband wafer was fabricated into a DFB laser array to characterize the wafer performance. Single-mode DFB emission between 5.8 and 9.9 μm under pulsed-mode operation (200 ns pulse width, 250 kHz repetition rate) is obtained from a 3 mm long cavity laser array with both facets AR-coated with 1300 nm Y_2O_3. As shown in Fig. 1(d), the threshold current is relatively flat between 5.9 and 9.2 μm, which indicates a flat gain at the threshold. The output power varies across the array due to the difference in slope efficiency, which depends on the internal quantum efficiency, the number of stages of the subcore, and the photon energy. The maximum peak power output is about 500 mW per facet at a wavelength of 7.0 μm, and most DFB lasers have a power output above 200 mW, which is higher than previous demonstrations [6,11]. The wafer is subsequently used for the development of a monolithic tunable laser with a single emitting aperture.

Figure 2(a) shows the schematic structure of an eight-laser SGDFB laser array integrated with an on-chip beam combiner. Each SGDFB laser is designed to target a certain MIR wavelength range by varying its grating period. One SGDFB laser is selected at a time for operation. The beam combiner is of a tree-array design, with s-bend waveguides and three stages of 2 × 1 junctions. A key concern for the beam combiner layout is to increase the output power by decreasing the fundamental-mode transmission loss. The transmission loss comes from the scattering loss of s-bend waveguides and coupling loss at each 2 × 1 junction.

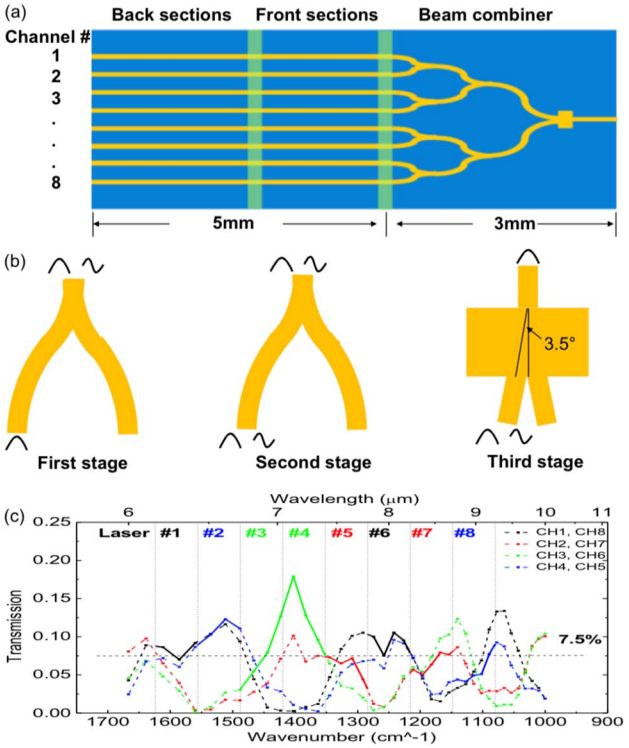

Fig. 2. (a) Schematic structure of the wavelength-tunable QCL source with monolithically integrated SGDFB laser array and beam combiner. (b) The transverse-mode evolution in the three stages of the beam combining. (c) The simulated fundamental-mode power transmission of the beam combiner as a function of wavenumber for the eight input waveguide channels (dash line). The selected channel for each laser is highlighted by a solid line.

The laser array has a separation of 120 μm, which is the minimum space for convenient wire bonding for each laser. The waveguide loss of *s*-bend waveguides decreases as the bending radius increases. However, in order to conserve the total length of the beam combiner section to 3 mm, the bending radius of the *s*-bend waveguides is set to 1600 μm, which gives a simulated scattering loss below 5% using the beam propagation method.

Figure 2(b) illustrates the transverse-mode evolution in the beam combiner for a fundamental mode launched from channel #1. After the first *Y* junction, there are both fundamental and higher-order modes (primarily first-order mode) existing inside the output waveguide. After the second *Y* junction, part of the power in the first-order mode is transferred back to the fundamental mode, causing interference with the fundamental mode excited by the fundamental-mode portion of the input. The interference effect increases or decreases the fundamental-mode transmission depends on the input wavelength and the geometry of the coupling waveguide, which is related to the input channel position. The last two waveguides in the tree array are combined using a 100 μm wide and 82 μm long slab waveguide. Both the fundamental and first-order mode inputs expand freely inside the slab waveguide before coupling to the output waveguide. A fundamental-mode input remains primarily the fundamental mode due to a small angle of 3.5° between the output and input waveguides. However, when the input is a first-order mode, the beam expands as a dual lobe inside the slab waveguide, which gives minimal overlap with the output waveguide. This means that

the beam combiner design acts a mode filter, allowing only the fundamental mode to be transmitted to the final output facet. Overall, the fundamental-mode power transmission depends on the wavelength and input channel position. For the laser ridge width of 10 μm, the power transmission of the fundamental mode for each input channel is simulated separately as a function of input wavelength between 6 and 10 μm.

Figure 2(c) shows the wavelength-dependent fundamental-mode power transmission for each channel. Due to symmetry of the structure, channels #1, #2, #3, and #4 have the same transmission as a function of wavelength as channels #8, #7, #6, and #5, respectively. For example, the laser beam launched from channel #1 always couples from the left branch of 2 × 1 junctions, and the beam launched from channel #8 always couples from the right branch of 2 × 1 junctions. Because of the interference effect, the overall power transfer to the output facet shows resonant features that can either increase or decrease the transmission as a function of the input waveguide position or wavelength. Laser #1 (#8) is designed to have the shortest (longest) wavelength emission. There are spectral regions similar in width to the targeted spectral region of each tunable laser (65 cm^{-1}) in which the beam combiner has increased the transmission. Based on the simulation, we have coupled the tunable lasers to the beam combiner channels that maximize the transmission over the specific laser tuning range instead of simply coupling the lasers to the combiner channels in an ascending order. For example, laser #2 is coupled to channel 4 instead of channel 2. Figure 2(c) shows that channel 4 has a five times higher power transmission than channel 2 within the designed tuning range of laser #2 (1555 – 1490 cm^{-1}). Overall, lasers #1, #2, #3, #4, #5, #6, #7, and #8 are coupled to beam combiner channels 1, 4, 3, 6, 2, 8, 7, and 5, respectively. Assuming a transparent waveguide, the simulated power throughput averages 7.5%.

The beam combiner is made from the same active waveguide as the lasers, so the output power can be increased significantly by applying the current to the beam combiner. However, the extent of amplification is limited by self-lasing of the beam combiner section. This causes excessive optical feedback into the tunable laser, which can affect the tuning behavior and spectral purity. As a result, a broadband AR coating on the front facet of the beam combiner is necessary to inhibit the self-lasing. In [7], a broadband AR coating between 6–10 μm was obtained using a multilayer coating of ZnS/YF_3. However, the multilayer structure has a large total thickness, and the thickness of each layer is difficult to control. Broadband trilayer AR coatings of $Al_2O_3/Si/Al_2O_3$ and bilayer coatings of $ZnSe/YF_3$ have been demonstrated in the spectral regions of 3–4 μm and 7–11 μm, respectively [5,12]. Here, we design a broadband AR coating for 6–10 μm using a double-layer structure of $ZnSe/MgF_2$ deposited by ion beam deposition. The reflectivity of the facet coating can be simulated with a transfer matrix method [13]. Figure 3(a) shows the simulated maximum reflectivity between 6 and 10 μm as a function of the ZnSe and MgF_2 layer thicknesses. The optimum thickness is found to be 800 nm ZnSe and 1400 nm MgF_2, but a high-quality AR coating with less than 2% reflectivity can be achieved with a wide range of layer thicknesses. Transmission of the deposited AR-coating film on an InP substrate is measured by a Fourier transform infrared (FTIR) spectrometer. The reflectivity between 6 and 10 μm is measured to be below 2% and the minimum reflectivity is as low as 0.1%, as shown in Fig. 3(b).

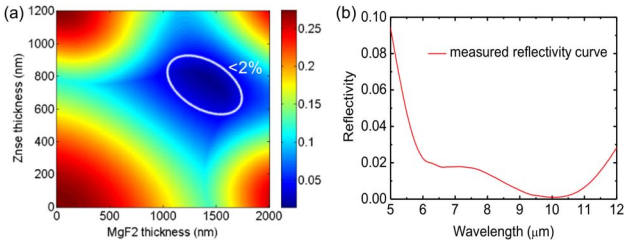

Fig. 3. (a) Simulated maximum reflectivity between 6 and 10 μm as a function of the MgF_2 and ZnSe film thicknesses. The coating sequence is a laser facet/ZnSe/MgF_2. The enclosure inside the white circle is a region where the maximum reflectivity is less than 2%. (b) The measured reflectivity curves of the AR coating consisting of 800 nm ZnSe and 1400 nm MgF_2.

The fabrication of the beam-combined tunable array laser source starts with electron beam lithography for defining the sampled gratings on top of the grating layer. A given SGDFB laser has two sections, each with a broad, comb-like reflectivity curve of different wavelength spacings. The product of these curves leads to a strong reflectivity at a single wavelength. An injected DC bias locally changes one of the SGDFB section temperatures, which leads to a change of the modal refractive index in that section. This causes a shift in the sampled grating reflectivity curve, and the SGDFB output wavelength is tuned via the Vernier effect. This mechanism is described in more detail in [8]. For this demonstration, each section is made up of 16 repeated grating bursts, with a spacing of 145.7 and 157.3 μm for the front and back sections of the SGDFB lasers, respectively. The estimated tuning step size is about 10 cm^{-1}. The grating period for each laser is designed as described earlier, such that Laser #1 (#8) is designed to have the shortest (longest) wavelength emission. The grating number per sampling period of 16, 16, 15, 15, 14, 14, 13, and 13 from Laser #1 to Laser #8 is determined to target a designed tuning range of 65 cm^{-1} for each SGDFB laser.

After the sampled grating definition, a regrowth of 4 μm low-doped InP cladding (Si, ∼2×10^{16} cm^{-3}) and 1 μm high-doped InP cap layer (Si, ∼5×10^{18} cm^{-3}) is performed by low pressure metalorganic chemical vapor deposition (MOCVD). The wafer is subsequently processed into double-channel waveguides with a ridge width of 10 μm in a similar way to [11]. A 12 μm deep-ridge waveguide is dry etched with a "$Cl_2/Ar/H_2$" chemistry to preserve the precise shape of the beam combiner region. Before the device was mounted epilayer-side up on a copper heat sink, the front facet of the beam combiner section is AR coated, as described above. A portable tunable laser system that contains three independent drivers to inject pulse/DC currents was built to test the tunable laser chip. The system also contains two 1 × 8 multiplexers to select the laser array pair to be driven. All measurements were performed using the tunable laser system at ambient room temperature with the internal thermoelectrically cooled (TEC) stage regulated at 15°C. The laser array operates in pulsed mode (75 ns pulse width, 500 kHz repetition rate), with the addition of DC biases to the different sections to tune the lasers' emission wavelengths. Spectral measurements were performed with a Bruker FTIR spectrometer at a resolution of 0.125 cm^{-1}. Figure 4 shows the combined tuning of 529 cm^{-1} between 6.1 and 9.2 μm for the light coming out of the single aperture of the beam combiner. High side-mode suppression ratios (SMSR) of 25–30 dB are achieved for most conditions, limited by the noise

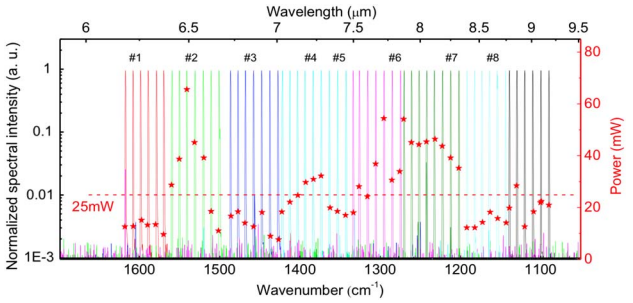

Fig. 4. Overlay plot of the compiled tuning spectra of the eight SGDFB lasers emitting from a single aperture and the measured output power. There are eight sets of peaks, represented in different colors corresponding to laser #1 through #8, respectively.

floor of the measurement system. Continuous scanning is not required due to the electric tuning inherent to the monolithic laser chip, and any emission wavelength can be rapidly recalled by setting the calibrated DC currents, which can be realized with the tunable laser system. The wavelength repeatability is measured to be better than 0.1 cm^{-1} when repeatedly turning on and off a selected laser. The high stability is attributed to a well-regulated TEC temperature and precisely controlled driving currents.

An aspheric lens with a diameter of 4 mm (C037TME-F from Thorlabs, MA) is placed in front of the laser chip to generate a collimated beam for power measurement. The average power as a function of wavelength is measured by scanning the laser from 6.1 to 9.2 μm. The SGDFB laser duty cycle is 3.75%, which is used to calculate the peak power per pulse. As shown in Fig. 4, the mean peak power is 25 mW with a range from 8 to 65 mW. The output power is one order of magnitude higher than previous demonstrations; this is largely attributed to the increased laser gain, the customized laser positions, and the broadband AR coating.

The collimated laser beam shape as a function of wavelength is measured by using the laser to directly illuminate a type-II superlattice-based long-wavelength infrared focal plane array (FPA) at a distance of 450 mm [14]. The laser was scanned between 6.1 and 9.2 μm with a step of 1 cm^{-1}. As shown in Fig. 5(a), a single bright spot is achieved, independent of which laser is active, with a spot diameter of 1.5–2.4 mm. This is attributed to the beam-combiner design that can maximize the transmission of the fundamental mode and filter out any higher-order modes. Figure 5(b) shows the angular displacement with respect to the beam center as a function of wavelength. The beam displacement never exceeds 1.6 mrad (0.1°), and is normally below about 1.0 mrad. This is attributed to the monolithic nature of the laser source, which contains a single-emission aperture and no moving parts. The low-beam steering addresses a major drawback of external cavity tunable lasers, which often show a large beam steering during wavelength tuning [15].

In conclusion, we have developed a high-performance, broadly tunable QCL source between 6.1 and 9.2 μm with up to 65 mW output power by increasing the gain of the heterogeneous broadband wafer, optimizing the waveguide design, and using a broadband AR coating. Future development is possible by implementing super-structure gratings to compensate the exact gain shape of the wafer. With our tunable laser system, random wavelength access and fast tuning are demonstrated with good stability due to the monolithic nature of the laser source. Such desirable

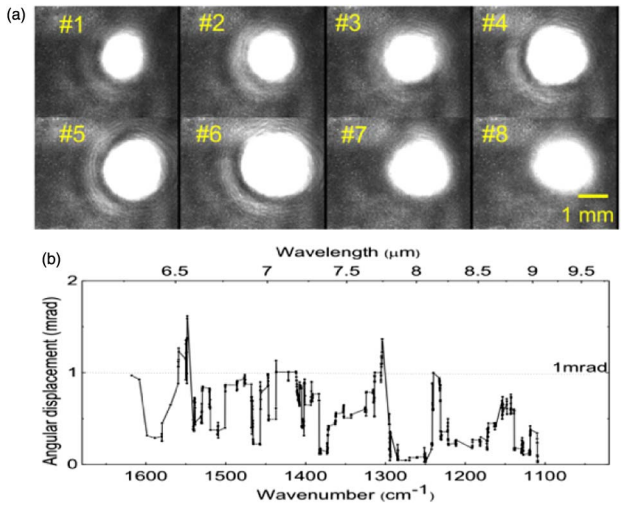

Fig. 5. (a) Typical beam shape measured by an infrared FPA for a beam combiner pumped by lasers #1–#8, showing mostly fundamental-mode operation for each laser. (b) The angular displacement as a function of wavelength as the laser wavelength is scanned over the full tuning range.

characteristics will enable new strategies and opportunities for MIR spectroscopy and chemical sensing.

Funding. U.S. Department of Homeland Security (DHS) (HSHQDC-13-C-00034).

Acknowledgment. The authors would like to acknowledge the support of all the involved program managers. The published material represents the position of the author(s) and not necessarily that of the Department of Homeland Security.

REFERENCES

1. J. Faist, F. Capasso, D. L. Sivco, C. Sirtori, A. L. Hutchinson, and A. Y. Cho, Science **264**, 553 (1994).
2. M. Razeghi, Q. Y. Lu, N. Bandyopadhyay, W. Zhou, D. Heydari, Y. Bai, and S. Slivken, Opt. Express **23**, 8462 (2015).
3. Q. Y. Lu, Y. Bai, N. Bandyopadhyay, S. Slivken, and M. Razeghi, Appl. Phys. Lett. **97**, 231119 (2010).
4. C. Gmachl, D. L. Sivco, J. N. Baillargeon, A. L. Hutchinson, F. Capasso, and A. Y. Cho, Appl. Phys. Lett. **79**, 572 (2001).
5. A. Hugi, R. Terazzi, Y. Bonetti, A. Wittmann, M. Fischer, M. Beck, J. Faist, and E. Gini, Appl. Phys. Lett. **95**, 061103 (2009).
6. N. Bandyopadhyay, M. Chen, S. Sengupta, S. Slivken, and M. Razeghi, Opt. Express **23**, 21159 (2015).
7. F. Xie, C. Caneau, H. Leblanc, M. T. Ho, and C. Zah, Opt. Lett. **40**, 4158 (2015).
8. S. Slivken, N. Bandyopadhyay, S. Tsao, S. Nida, Y. Bai, Q. Y. Lu, and M. Razeghi, Appl. Phys. Lett. **100**, 261112 (2012).
9. S. Kalchmair, R. Blanchard, T. S. Mansuripur, G. M. de Naurois, C. Pfluegl, M. F. Witinski, L. Diehl, F. Capasso, and M. Loncar, Opt. Express **23**, 15734 (2015).
10. A. S. Diba, F. Xie, B. Gross, L. C. Hughes, C. E. Zah, and F. Moshary, Opt. Express **23**, 27123 (2015).
11. W. J. Zhou, N. Bandyopadhyay, D. H. Wu, R. McClintock, and M. Razeghi, Sci. Rep. **6**, 25213 (2016).
12. S. Riedi, A. Hugi, A. Bismuto, M. Beck, and J. Faist, Appl. Phys. Lett. **103**, 031108 (2013).
13. P. Baumeister, *Optical Coating Technology* (SPIE, 2004).
14. P. Y. Delaunay, B. M. Nguyen, D. Hoffman, E. K. W. Huang, and M. Razeghi, IEEE J. Quantum Electron. **45**, 157 (2009).
15. C. A. Kendziora, R. Furstenberg, M. Papantonakis, V. Nguyen, and R. A. McGill, Proc. SPIE **9836**, 98362G (2016).